Control of ultrafast photocurrent in twisted bilayer graphene by circularly polarized few-cycle lasers

Jiayin Chen, Candong Liu,* Zhinan Zeng, and Ruxin Li
State Key Laboratory of High Field Laser Physics and CAS Center for Excellence in Ultra-intense Laser Science, Shanghai Institute of Optics and Fine Mechanics (SIOM), Chinese Academy of Sciences (CAS), Shanghai 201800, China
and Center of Materials Science and Optoelectronics Engineering, University of Chinese Academy of Sciences, Beijing 100049, China

(Received 16 November 2021; revised 13 January 2022; accepted 14 January 2022; published 26 January 2022)

We perform nonperturbative calculations of light field induced current in twisted bilayer graphene (tBLG) irradiated by a circularly polarized (CP) few-cycle laser pulse. The strong-field electron dynamics is simulated within a single-particle picture by two complementary approaches, including the velocity-gauge density-matrix equation and the length-gauge time-dependent Schrödinger equation, which both combine a tight-binding model for describing tBLG electronic structures. The two theoretical approaches yield the same result in the context of studying the carrier-envelope phase (CEP) and laser intensity dependent photocurrent. We show that the measured current exhibits a sinusoidal dependence on CEP of CP driving fields, with the sine phase determined by the electrode orientation with respect to the tBLG lattices. Moreover, it has been proven that an important reversal of the photocurrent direction occurs as the driving optical field strength increases to the strong-field regime, which cannot appear in the monolayer or conventional AA- and AB-stacked bilayer graphene. Based on the analysis of the conduction band population, we successfully identify that such current direction reversal in tBLG mainly originates from the interference of multichannel electron transition among two conduction bands and four valence bands closest to the Fermi level. Our results may pave the way toward investigation of nonlinear optical response in layered materials, and might provide insight for the design of future ultrafast optoelectronic devices.

DOI: 10.1103/PhysRevB.105.014309

I. INTRODUCTION

Important advances in ultrafast laser technology enable us to coherently manipulate electron motion in solids on the subfemtosecond timescale by making use of optical waveforms of light. The inducing photocurrent in semiconductors or dielectrics and its precise control forms the foundation in lightwave electronics [1,2]. In particular, using intense optical field can boost the possibility of ultrafast carrier excitation in wideband materials, which is conducive to building rapid electronic switches in the petahertz regime [3], since the temporal scale of electron density oscillation is inversely proportional to the band gap.

A pioneering work on the electronic signal manipulation by a few-cycle optical waveform is the experimental realization of carrier envelope phase (CEP) control of optical field induced current in fused silica [4]. Later, it was demonstrated that similar semimetallization can occur not only in several other wide band gap insulators subjected to strong optical fields [5,6], but also in a narrower band gap semiconductor exposed to a substantially lower light intensity [7]. For the anisotropic crystals, an *ab initio* simulation predicts that the phase of the photocurrent can shift with the driving laser polarization [8], which is subsequently demonstrated by a series of experimental observations [9].The coherent CEP control of electric currents in these kinds of measurement can be either explained by the dynamic formation of localized Wannier-Stark states [4] or attributed to interference between different multiphoton excitation channels [10]. Additionally, coherent control using two-color beams of the same vector mode provides the capability to achieve the complete vectorial arrangement of currents in a semiconductor [11].

The ultrafast control of field-induced current in graphene, a typical Dirac material, has also been intensively studied. Different from dielectrics, graphene with zero band gap property exhibits an important interband transition, which can be strongly affected by intraband motion, especially for higher optical fields [12]. A striking reversal of current direction is observed in the strong-field regime owing to field-driven Landau-Zener-Stückelberg (LZS) interference on a suboptical-cycle timescale [13]. Further experiment and theory shows that this current can be controlled by the electrode distance and the direction of initial current injection [14], as well as the chirp rate of the driving pulse [15].

As another important Dirac material, twisted bilayer graphene (tBLG) has recently attracted lots of interest as it brings about many novel physical phenomena such as magic-angle superconductivity [16] and correlated insulator behavior [17]. Compared with monolayer graphene (MLG), tBLG has an additional freedom of lattice mismatch between two atomic layers, leading to the formation of a superlattice and substantial modification to electronic structures. The previous study on light-tBLG interaction is mainly concentrated on cases with relatively weak laser intensity [18,19], for which the physical mechanism is dominated by the band structure

*cdliu@siom.ac.cn

around the Fermi level in the low-energy region. Although the nonlinear process, such as high-order harmonic generation in tBLG [20,21], was partly investigated very recently, the other strong-field optical response of tBLG has not yet been extensively discussed. The superlattice of tBLG usually corresponds to the smaller folding Brillouin zone where the electron could be easily accelerated to the edge under strong fields. Simultaneously, the coupling effect among multiple bands would become crucial. Hence, it is expected that light waveform control of ultrafast dynamics in tBLG will contain unique contents, particularly in the strong-field regime.

In this work, we calculate the optical field induced current in commensurate tBLG with large twisted angles. The few-cycle circularly polarized (CP) pulse with a stabilized CEP is used to steer two-dimensional (2D) electron motion that can efficiently prevent the LZS interference. This treatment is helpful to highlight the other interference phenomena involved in the tBLG photocurrent generation. We perform nonperturbative calculation of electron dynamics by separately solving the velocity-gauge Liouville–von Neumann equation and the length-gauge time-dependent Schrödinger equation (TDSE), both taking into account the complete tBLG electronic structures instead of the widely used low-energy continuum model [22]. The field-induced current is investigated as a function of several parameters, i.e., CEP, electrode orientation, and field strength of light pulse, with the particular emphasis on the influence of the latter. We show that field strength dependent current exhibits a direction reversal which cannot occur in monolayer graphene or conventional AA- and AB-stacked bilayer graphene. The underlying physical mechanism is further interpreted by the analysis of k-space conduction band population, and a multichannel interference process associated with electron transition between different energy bands is revealed.

II. THEORETICAL METHODS

We begin by describing how to construct tBLG with two MLG sheets. Generally, stacking two MLGs on top of each other can lead to different configurations. The bilayer system where the lattices of two graphene layers are completely overlapped is termed AA stacking. When we only rotate the top layer of AA stacking by 60 ° around an axis passing through a pair of coincident carbon atom sites, the resulting system is AB stacking. In this case, one of the two sublattices of one layer lies in the center of the honeycomb structure of the other layer. If continuing to rotate counterclockwise the top layer of AB-stacked form by a special angle θ around the same axis, we can obtain an important tBLG known as the commensurate structure, which maintains the superlattice translation symmetry and thus is more convenient for theoretical treatment. Such commensurate rotation angle should satisfy [23]

$$\cos\theta = \frac{3m^2 + 3mr + r^2/2}{3m^2 + 3mr + r^2}, \tag{1}$$

where m and r are coprime positive integers. In this work, we mainly focus on the particular commensurate structure given by $m = 1$ and $r = 1$, yielding the minimal primary supercell. The other commensurate structures are simply discussed at the end.

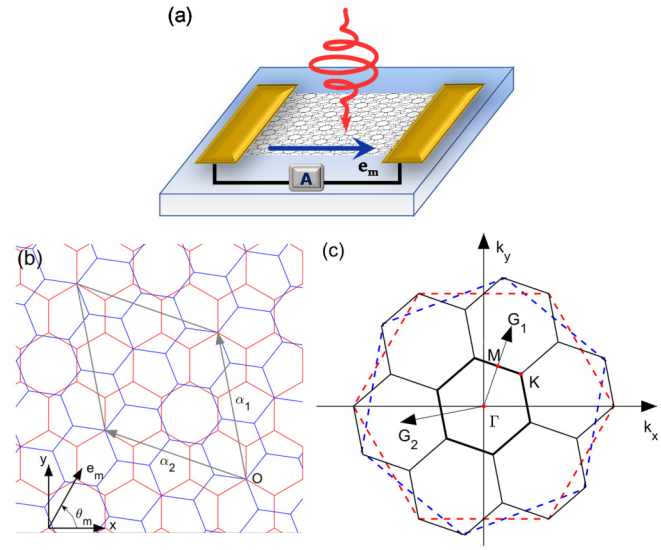

FIG. 1. (a) Schematic setup of generating photocurrent by circularly polarized light. (b) The in-plane lattice structure of commensurate tBLG with a twisted angle $\theta \approx 21.8^\circ$ ($m = 1, r = 1$). The α_1 and α_2 are the basis vectors of the superlattice. The vector $\mathbf{e_m}$ represents electrode orientation, described by a polar angle θ_m. (c) The schematic of BZ corresponding to panel (b). The first BZ of the top layer (blue dashed hexagon) rotates $\theta \approx 21.8^\circ$ counterclockwise relative to the first BZ of the bottom layer (red dashed hexagon). The seven smaller hexagons in black are the BZ of superlattice tBLG. $\mathbf{G}_1$ and $\mathbf{G}_2$ are the reciprocal lattice primitive vectors.

A typical schematic of photocurrent measurement setup is shown in Fig. 1(a). The charge carriers generated by the tBLG under illumination of laser pulses can move toward two electrodes, and therefore a photocurrent can be collected. Due to the anisotropic of tBLG driven by CP pulses, the arrangement of two electrodes should be carefully considered. We describe the electrode orientation by a direction vector $\mathbf{e_m}$, as shown in Fig. 1(a). The lattice structure of the tBLG ($m = 1, r = 1$) is illustrated in Fig. 1(b), where the parallelogram gives the unit supercell spanned by two basis vectors ($\boldsymbol{\alpha}_1, \boldsymbol{\alpha}_2$). Here, we express the electrode orientation $\mathbf{e_m}$ by a polar angle θ_m as $\mathbf{e_m} = (\cos\theta_m, \sin\theta_m)$. Figure 1(c) shows the corresponding Brillouin zone (BZ) of the bottom layer (red dashed hexagon) and the top layer (blue dashed hexagon), together with the first BZ of tBLG given by the central small black solid hexagon. The reciprocal lattice primitive vectors can be chosen as

$$\begin{pmatrix}\mathbf{G}_1\\ \mathbf{G}_2\end{pmatrix} = \frac{4\pi}{3|\alpha_1|^2}\begin{pmatrix}2 & -1\\ -1 & 2\end{pmatrix}\begin{pmatrix}\alpha_1\\ \alpha_2\end{pmatrix}. \tag{2}$$

The detailed description on the tBLG lattice and BZ can be found in our recent work [21].

When the tBLG is exposed into a laser field, its electron dynamics can be modeled by a time-dependent Schrödinger equation (TDSE) within single-electron approximation,

$$i\frac{\partial}{\partial t}\psi(\mathbf{r}, t) = [H_0 + \mathbf{r}\cdot\mathbf{E}(t)]\psi(\mathbf{r}, t), \tag{3}$$

where H_0 is the field-free Hamiltonian described by the tight-binding model [21,24,25], and we adopt the length-gauge

interaction expression containing the external electric field $\mathbf{E}(t)$. Unless otherwise indicated, atomic units (a.u.) are used throughout: $e = \hbar = m_e = 1$, where e and m_e are the electron charge and mass, respectively. Since the position operator $\mathbf{r}$ breaks translational symmetry, we should construct an ansatz for solving Eq. (3) within a frame of crystal momentum moving with the vector potential $\mathbf{A}(t) = -\int_{-\infty}^{t} \mathbf{E}(t')dt'$. For an initial crystal momentum $\mathbf{k}_0$, the wave function can be expanded as

$$\psi_{\mathbf{k}_0}(\mathbf{r}, t) = \sum_i c_i^{\mathbf{k}_0}(t) B_{i,\mathbf{k}(t)}(\mathbf{r}), \tag{4}$$

with the time-dependent momentum $\mathbf{k}(t) = \mathbf{k}_0 + \mathbf{A}(t)$. Here, the basis function $B_{i,\mathbf{k}(t)}(\mathbf{r})$ denotes the Bloch sum of the carbon $2p_z$ orbital, and i labels one atom in the primary supercell of tBLG. Using the ansatz (4), we can obtain the temporal evolution for coefficients $c_i^{\mathbf{k}_0}(t)$ in a matrix form as

$$i\frac{\partial}{\partial t}\mathbf{C}^{\mathbf{k}_0}(t) = \mathbf{H}(\mathbf{k})\mathbf{C}^{\mathbf{k}_0}(t), \tag{5}$$

where expansion coefficients form a column vector $\mathbf{C}^{\mathbf{k}_0}(t) = [c_1^{\mathbf{k}_0}(t), c_2^{\mathbf{k}_0}(t), \ldots, c_l^{\mathbf{k}_0}(t)]^T$, and the tight-binding Hamiltonian matrix $\mathbf{H}(\mathbf{k})$ consists of elements $H_{ij}(\mathbf{k}) = \langle B_i|H_0|B_j\rangle$ in the representation of the atomic orbital basis. Taking tBLG ($m = 1$, $r = 1$) as an example, we can choose the parallelogram in Fig. 1(b) as the primary unit cell which includes 28 atoms to construct the tight-binding Hamiltonian, therefore generating 28 energy bands if only one $2p_z$ orbital is assigned to one carbon atom. The detailed derivation for obtaining Eq. (5) is given in Appendix A.

In order to calculate the photocurrent, we need information on the population of electrons occupying an arbitrary energy band. Thus, it is necessary to expand the wave function in valence- and conduction-band representation as

$$\psi_{\mathbf{k}_0}(\mathbf{r}, t) = \sum_n b_n^{\mathbf{k}_0}(t)\phi_{n,\mathbf{k}(t)}(\mathbf{r}), \tag{6}$$

where $\phi_{n,\mathbf{k}(t)}(\mathbf{r})$ is the nth eigenstate of the field-free Hamiltonian H_0. If we introduce a column vector notation $\mathbf{C}_B^{\mathbf{k}_0}(t) = [b_1^{\mathbf{k}_0}(t), b_2^{\mathbf{k}_0}(t), \ldots, b_l^{\mathbf{k}_0}(t)]^T$, those coefficients in two different representations are related by a unitary transformation $\mathbf{C}_B^{\mathbf{k}_0}(t) = \mathbf{U}_{\mathbf{k}(t)}^{\dagger}\mathbf{C}^{\mathbf{k}_0}(t)$, where $\mathbf{U}_{\mathbf{k}(t)}$ is a unitary matrix constructed by arranging the eigenvectors of $\mathbf{H}(\mathbf{k})$ in columns. The time-dependent population at a fixed $\mathbf{k}_0$ for the nth band is then given by $\rho_n(\mathbf{k}_0, t) = |b_n^{\mathbf{k}_0}(t)|^2$.

We numerically solve Eq. (5) under a set of different initial conditions that only one of the valence band (VB) states is fully occupied for each time solving Eq. (5). By summing the contribution of residual conduction band (CB) population obtained from each individual propagation of Eq. (5), we can express the total transferred charge density as [13]

$$Q \propto \sum_{s\in\mathrm{VB}, n\in\mathrm{CB}} \int_{\mathrm{BZ}} \rho_n^s(\mathbf{k}_0, +\infty)\mathbf{e_m} \cdot \nabla_{\mathbf{k}_0}\varepsilon_n(\mathbf{k}_0)d\mathbf{k}_0, \tag{7}$$

where the index s indicates that the initial electron occupies the sth VB, and ρ_n^s represents the residual nth CB population resulted from the s-occupied initial condition. Here, $\mathbf{e_m} \cdot \nabla_{\mathbf{k}_0}\varepsilon_n(\mathbf{k}_0)$ describes that carriers move toward the electrode direction with the group velocity determined by the gradient of the nth CB energy dispersion $\varepsilon_n(\mathbf{k}_0)$. We point out that the above treatment is equivalent to fulfilling all VBs, and simultaneously cancels out the unphysical transitions forbidden by the Pauli exclusion principle.

To make the simulation more convincing, we also use density-matrix models for describing strong-field electron dynamics. The Liouville–von Neumann equation in the velocity gauge is solved to obtain the total current density, whose expression is given by

$$\mathbf{J}(t) \propto \int_{\mathrm{BZ}} \mathrm{Tr}\{\hat{\rho}(t)[\hat{\mathbf{p}}(\mathbf{k}) + \mathbf{A}(t)]\}d^2\mathbf{k}, \tag{8}$$

where $\hat{\rho}(t)$ represents the temporal evolution of the density matrix, and $\hat{\mathbf{p}}(\mathbf{k})$ is the momentum matrix. See Ref. [21] for details on equations and relevant matrix elements. From Eq. (8), we can define the time-dependent polarization $\mathbf{P}(t) = \int_{-\infty}^{t} \mathbf{J}(t')dt'$. For an ideal model that considers all possible relaxation mechanisms, the total transferred charge density is proportional to the value of field-induced polarization $\mathbf{P}(t)$ at a finite moment after the end of the laser pulse. However, since we do not consider the relaxation phenomena, the polarization will continue to oscillate after the laser pulse. To avoid this problem, we can follow Ref. [10] to calculate the transferred charge density as the average of $\mathbf{P}(t)$ during a time window,

$$Q \propto \frac{1}{\Delta t}\int_{t_f}^{t_f+\Delta t} \mathbf{P}(\tau) \cdot \mathbf{e}_m(\theta_m)d\tau. \tag{9}$$

We choose $t_f = 15$ fs and $\Delta t = 5$ fs throughout and find that simulation results are insensitive to the two parameters.

For both models, the net current yielded in the experimental measurement can be approximately regarded as proportional to Q if ballistic transfer of charge is simply assumed. We sample the Brillouin zone with a uniform grid along two nonorthogonal directions of the reciprocal lattice vectors, and then propagate the TDSE or density-matrix equation for each independent $\mathbf{k}$. The grid interval of crystal momentum and evolution time is fixed to $\delta k = 0.004$ a.u. and $\delta t = 0.2$ a.u.

III. RESULTS AND DISCUSSION

A. Dependence of photocurrent on CEP and field strength of light

The electron dynamics of tBLG in a strong-field regime is sensitive to the full electric-field waveform due to the fact that it usually occurs on the subfemtosecond timescale. This can result in light-induced current controlled by CEP of few-cycle driving lasers. In addition, we devote to a discussion on the CP field, which can steer electron motion along 2D spiraling trajectories. Thus, the above two factors suggest that we observe how CEP and electrode orientation affect photocurrent.

We consider tBLG excited by a 5-fs CP pulse with a central wavelength of 800 nm and a peak field strength of 2.5 V/nm. The coherent electron dynamics induced by the ultrashort pulse is faster than electron-electron scattering, which is typically on a tens of femtoseconds timescale. It is therefore reasonable to treat the fully coherent evolution and ignore the relaxation process in our model. Figure 2 shows the light field induced current as a function of CEP for using a left ($\varepsilon = -1$,

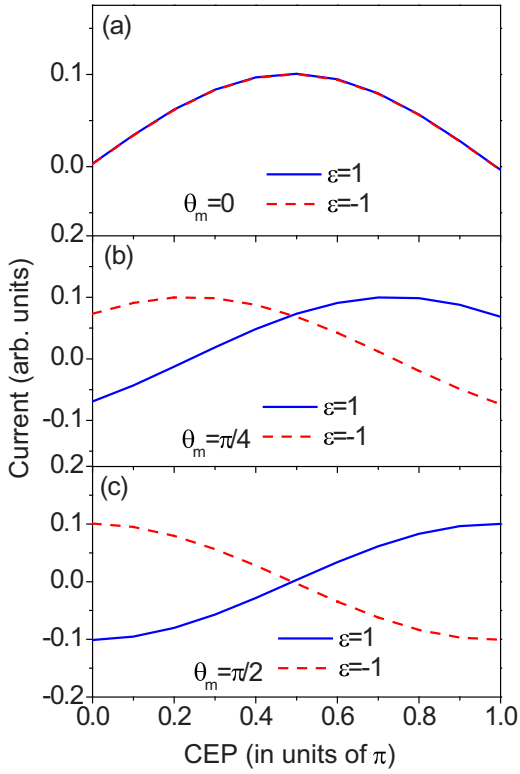

FIG. 2. The CEP-dependent current in tBLG driven by left ($\varepsilon = -1$, red dashed) or right ($\varepsilon = 1$, blue solid) CP laser pulse, with the electrode orientation set as (a) $\theta_{\mathbf{m}} = 0$, (b) $\theta_{\mathbf{m}} = \pi/4$, and (c) $\theta_{\mathbf{m}} = \pi/2$. The laser pulse centered at 800 nm has a duration of 5 fs and a peak field strength of 2.5 V/nm.

red dashed) or right ($\varepsilon = 1$, blue solid) CP laser, with the measurement taken at three different electrode orientation arrangements: (a) $\theta_{\mathbf{m}} = 0$, (b) $\theta_{\mathbf{m}} = \pi/4$, and (c) $\theta_{\mathbf{m}} = \pi/2$. One can see that with different $\theta_{\mathbf{m}}$ the CEP-dependent current exhibits a phase shift whose value can be directly extracted from Fig. 2 and is found to be equal to variations of $\theta_{\mathbf{m}}$, but with opposite direction for left and right CP pulses. These important features suggest that the transferred charge density (or current) can be simply fitted as $Q \propto \sin(\phi_{\mathrm{CEP}} - \varepsilon\theta_{\mathbf{m}})$. The expression represents that the experimental choice of electrode orientation relative to tBLG lattice is not crucial. For an arbitrary $\theta_{\mathbf{m}}$, we can always make current reach the maximal by adjusting the appropriate ϕ_{CEP}. We point out that although Fig. 2 is obtained by the density-matrix model, the TDSE approach can yield the same result, which is not shown here.

The result reported in Fig. 2 can be qualitatively interpreted by a semiclassical picture. Our tight-binding model for the tBLG ($m = 1, r = 1$) yields an almost linear dispersion around the Dirac points, $\mathbf{K}_D$. The first two almost degenerate conduction bands near the Fermi level can be approximately described as

$$E_c(\mathbf{k}) = v_{\mathrm{F}}|\mathbf{k} - \mathbf{K}_D| + \mu. \tag{10}$$

From the definition of the group velocity and the acceleration theorem, the light field induced current can be written as

$$\mathbf{J}(t) \propto \nabla_{\mathbf{k}} E_c[\mathbf{k} + \mathbf{A}(t)]|_{\mathbf{k}=\mathbf{K}_D}, \tag{11}$$

where only the contribution from the Dirac point is considered. Here for simplicity and analytical treatment, we employ the CP plane-wave vector potential,

$$\mathbf{A}(t) = A_0[\cos(\omega_0 t + \phi_{\mathrm{CEP}})\mathbf{e}_x + \varepsilon \sin(\omega_0 t + \phi_{\mathrm{CEP}})\mathbf{e}_y]. \tag{12}$$

Combing Eqs. (10)–(12), we get

$$\mathbf{J}(t) \propto \cos(\omega_0 t + \phi_{\mathrm{CEP}})\mathbf{e}_x + \varepsilon \sin(\omega_0 t + \phi_{\mathrm{CEP}})\mathbf{e}_y. \tag{13}$$

Considering the electrode orientation $\mathbf{e}_{\mathbf{m}} = \cos\theta_{\mathrm{m}}\mathbf{e}_x + \sin\theta_{\mathrm{m}}\mathbf{e}_y$, the net current in the experimental measurement can be approximately regarded as

$$Q \propto \int^{t_0} \mathbf{e}_{\mathbf{m}} \cdot \mathbf{J}(t)dt \sim \sin(\omega_0 t_0 + \phi_{\mathrm{CEP}} - \varepsilon\theta_{\mathrm{m}}), \tag{14}$$

which is consistent with the fitting result of numerical calculation in Fig. 2. We denote the initial phase shift as $\theta_0 = \omega_0 t_0$, whose value is not important and is determined by the specific case. Consequently, the condition for the crossing of the red and blue curves Fig. 2 is given by

$$\sin(\theta_0 + \phi_{\mathrm{CEP}} - \theta_{\mathrm{m}}) = \sin(\theta_0 + \phi_{\mathrm{CEP}} + \theta_{\mathrm{m}}). \tag{15}$$

It follows that the CEP value of the crossing point is $\phi_{\mathrm{CEP}} = \frac{\pi}{2} - \theta_0$, independent of electrode orientation.

The laser field strength is an important parameter that determines the electron transition mechanism. The increasing of the optical field is usually accompanied by the conversion in electron transition dynamics from the perturbative to the strong-field regime. We now turn to scanning the optical field to clarify the variation trend of photocurrent in tBLG, and to reveal the critical field strength at which a different transition mechanism occurs.

For comparison, we investigate photocurrent generation in four different graphene configurations, i.e., MLG, conventional AA- and AB-stacking bilayer graphene, and tBLG ($m = 1$, $r = 1$), which are excited by CEP-stabilized few-cycle 5-fs CP laser pulses centered at 800 nm with a peak field ranging from 0 to 4 V/nm. Figure 3 shows the current as a function of optical peak field strength E_0, calculated for MLG (black solid), AA-stacking bilayer (blue dashed), AB-stacking bilayer (red dot), and tBLG (olive dashed dot), obtained from (a) the density-matrix model and (b) the TDSE model. In the simulation, the CEP and electrode orientation are matched such that the photocurrent reaches the maximum for each different material. For the tBLG, we choose $\theta_{\mathbf{m}} = 0$ and CEP $\phi_{\mathrm{CEP}} = \pi/2$. One can see from Figs. 3(a) and 3(b) that both models yield almost consistent results. Note that calculation results from Eqs. (7) and (9) are rescaled by multiplying a constant to make the two theoretical methods give the same current value at $E_0 = 2.6$ V/nm for tBLG.

Several important characteristics can be found in Fig. 3. The current monotonically increases as a function of E_0 when $E_0 < 2.6$V/nm for all four graphene systems. This is the typical power-law characteristic in the weak-field regime

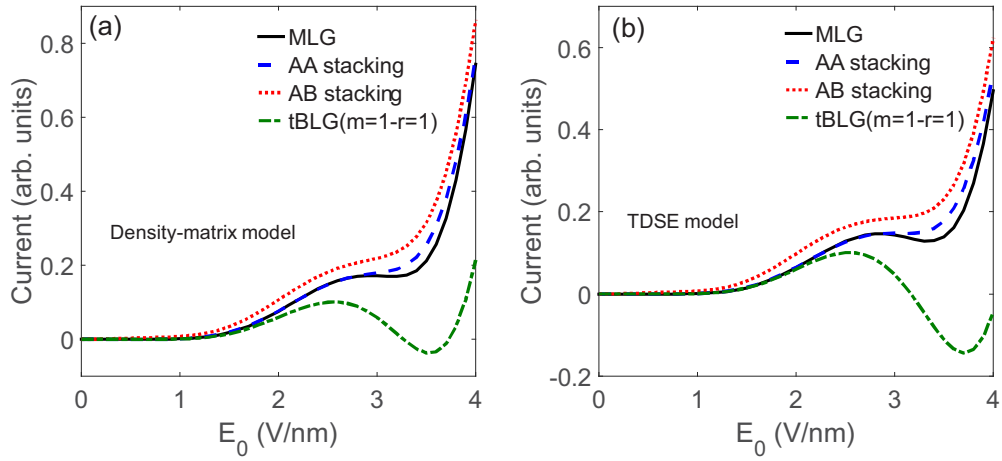

FIG. 3. The current in MLG (black solid), AA-stacking bilayer (blue dashed), AB-stacking bilayer (red dot), and tBLG (olive dashed dot), calculated as a function of the peak electric field strength E_0 using (a) the density-matrix model and (b) the TDSE model. The CP driving pulse has a central wavelength of 800 nm and a duration of 5 fs.

[26,27] where the perturbative theory holds and the light-matter interaction can be described by the photon-driven picture. Although the value 2.6 V/nm is approximately read from Fig. 3, it can be actually related with a characteristic energy formulated as an effective Rabi frequency. For the four graphene systems in Fig. 3, they have similar Dirac-cone dispersion with a slightly different Fermi velocity v_F around the K point. Following the acceleration theorem, the relevant electron dynamics along one direction can be qualitatively described by a two-level Rabi system [13], where the Rabi frequency is given by $\Omega_R = \frac{v_F E_0}{\sqrt{2}\omega_0}$ in atomic units. Here, the factor $\sqrt{2}$ rises from the circularly polarized pulse we study, and ω_0 is the central angular frequency of the driving pulse. The electron dynamics lies in the perturbative regime when the interaction strength is much less than the photon energy; i.e., $\Omega_R/\omega_0 \ll 1$. We consider the situation that light-graphene interactions start to deviate from the perturbative, but still do not enter into the strong-field regime. It is therefore reasonable to choose the middle position $\Omega_R/\omega_0 = 1/2$ as a definition of the critical field strength E_c, which gives $E_c = \frac{\omega_0^2}{\sqrt{2}v_F}$. With tight-binding structure parameters and the central driving photon energy $\hbar\omega_0 = 1.5$ eV employed here, we can estimate that the critical field strength for the four graphene systems is equal to $E_c \approx 2.6{-}2.9$ V/nm. Note that our model yields the Fermi velocity of MLG and AA/AB bilayers $v_F \approx 1$ nm/fs, and the Fermi velocity of tBLG ($m = 1,\ r = 1$) $v_F' \approx 0.9 v_F$.

When the optical field exceeds 2.6 V/nm, the dependence of current on E_0 exhibits a different relationship with the power law, representing that electronic dynamics gradually enters into the nonperturbative regime. In particular the current in tBLG shows nonmonotonic behavior such that even a reversal of current direction takes place at $E_0 \approx 3.2$ V/nm. In contrast, the current in MLG, and AA and AB stacking always stays positive with increasing the optical field strength.

We point out that the linearly polarized few-cycle pulse can also result in the reversal of current direction in MLG due to suboptical-cycle LZS interference [13]. Instead, CP light used here manipulates 2D electron motion, which prevents the intra-optical-cycle LZS, since only one transition event per cycle can occur. This 2D nature causes the direction of CP-induced current in MLG to not reverse [13]. The same physical picture can be also applied to AA- and AB-stacking bilayer graphene because their current curve shares the same variation trend as the one in MLG, while it fails for tBLG where the reversal still exists (see Fig. 3). The difference implies that there is another mechanism behind the reversal phenomenon in tBLG.

B. Calculation of k-resolved residual population of conduction bands

The analysis of residual CB population in tBLG is helpful to clarify the origin of photocurrent direction reversal, as manifested by Eq. (7). We have calculated the distribution of total CB population in the k space, which is defined as

$$\rho_c(\mathbf{k}_0) = \sum_{s\in \mathrm{VB}, n\in \mathrm{CB}} \rho_n^s(\mathbf{k}_0, +\infty). \tag{16}$$

Figure 4(a) shows the simulation result of $\rho_c(\mathbf{k}_0)$ at $E_0 = 3.5$ V/nm. Note that in our simulation the total population including all VBs and CBs at a fixed $\mathbf{k}_0$ is always equal to the VB number $N_{\mathrm{VB}} = 14$. Several ring patterns exist around the k-space Dirac point. Around one of the Dirac points in Fig. 4(a), we also indicate those resonances in black dashed (red dot) curves, corresponding to the energy difference between the lowest (the second lowest) CB and the highest (the second highest) VB equal to $n\hbar\omega_0$ ($n = 1, 2$), where $\omega_0 = 1.55$ eV is the central photon energy of the driving light. The rings are associated with one- and two-photon excitation, while the Landau-Zener transition is responsible for the central bright spot at the Dirac point.

It has been demonstrated by Fig. 2 that change of the driving pulse CEP by π only leads to the opposite sign of current. Consequently, the difference between currents generated by two CEPs $\phi_{\mathrm{CEP}} = \pi/2$ and $\phi_{\mathrm{CEP}} = -\pi/2$ can maintain the original sign of the current ($\phi_{\mathrm{CEP}} = \pi/2$) unchanged. In order to track clearly the current direction in the reciprocal space, we introduce $\Delta\rho_c(\mathbf{k}_0)$, defined as the difference in the

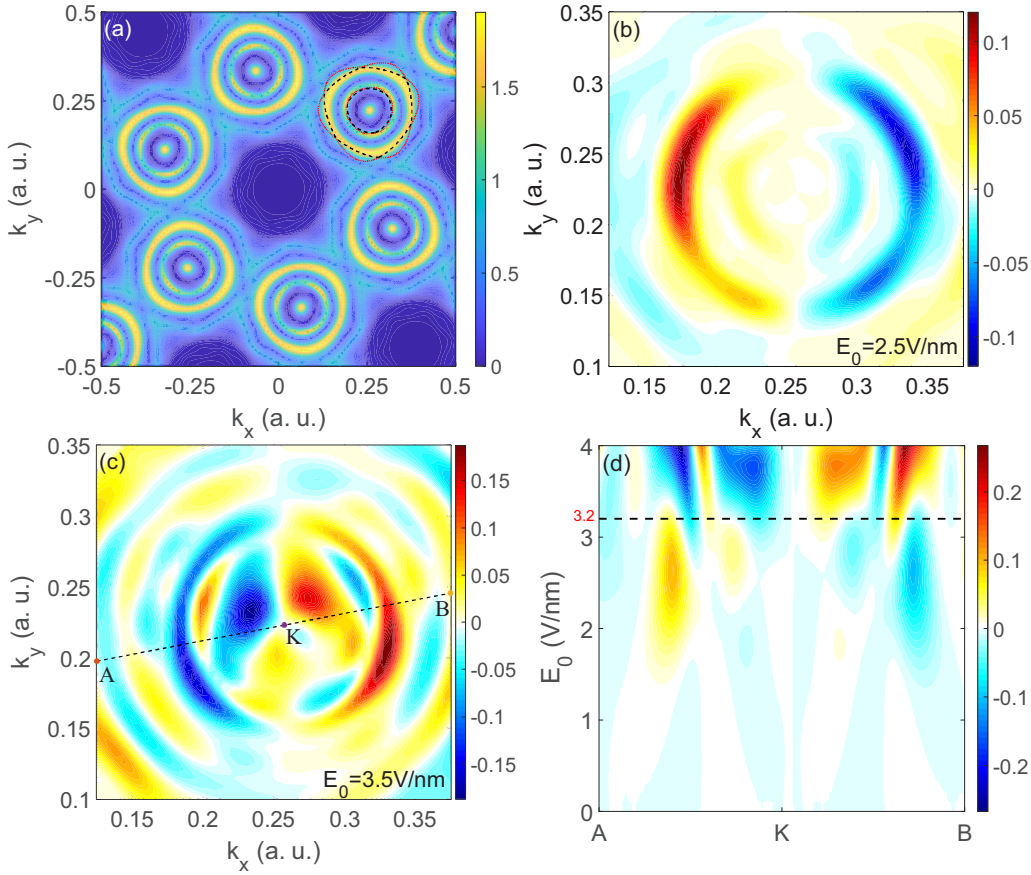

FIG. 4. (a) The k-resolved residual distribution of total CB population for $E_0 = 3.5\,\mathrm{V/nm}$. Black dashed (red dot) curves around one of the Dirac points represent resonances, where the energy difference between the lowest (the second lowest) CB and the highest (the second highest) VB is equal to photon energy $\hbar\omega_0$ or $2\hbar\omega_0$. (b), (c) The difference $\Delta\rho_c(\mathbf{k}_0)$ between the residual CB population resulting from excitation with $\phi_{\mathrm{CEP}} = \pi/2$ and $\phi_{\mathrm{CEP}} = -\pi/2$, plotted at two different peak field strengths (b) $E_0 = 2.5\,\mathrm{V/nm}$ and (c) $E_0 = 3.5\,\mathrm{V/nm}$. (d) Extracted $\Delta\rho_c(\mathbf{k}_0)$ along a straight line denoted by AKB in panel (c), calculated as a function of E_0. The black dashed line indicates the field strength $E_0 = 3.2\,\mathrm{V/nm}$ at which the current direction reverses. Other laser parameters are the same as in Fig. 3.

residual CB population between the excitation pulses with $\phi_{\mathrm{CEP}} = \pi/2$ and $\phi_{\mathrm{CEP}} = -\pi/2$. At $E_0 = 2.5\,\mathrm{V/nm}$, $\Delta\rho_c(\mathbf{k}_0)$ is plotted in Fig. 4(b), where we only show the vicinity of one Dirac point due to similar behavior at others. Evidently, the dominating positive area is located at the left side of the Dirac point. The asymmetric distribution of $\Delta\rho_c(\mathbf{k}_0)$ along the horizontal direction forms an observable current. For comparison, we increase the peak field strength to $E_0 = 3.5\,\mathrm{V/nm}$. Figure 4(c) shows the corresponding $\Delta\rho_c(\mathbf{k}_0)$, where the main positive area is changed to the right side of the Dirac point. The contrast gives direct evidence for the control of current direction by field strength.

We can further extract $\Delta\rho_c(\mathbf{k}_0)$ along a line that is chosen to pass through the Dirac point and be parallel to G_2, as denoted in Fig. 4(c), and calculate its variation with the field strength. The result is reported in Fig. 4(d). One can see that $\Delta\rho_c(\mathbf{k}_0)$ evolves almost monotonically until $E_0 = 2.6\,\mathrm{V/nm}$, representing the perturbation process in the weak-field limit. Along the vertical axis, it is also clear to identify a significant change in the sign of $\Delta\rho_c(\mathbf{k}_0)$ at the field strength $E_0 \approx 3.2\,\mathrm{V/nm}$, as indicated by the dashed line in Fig. 4(d). At this time, the interaction falls into the strong-field regime. Here the dashed-line positon matches well with the field strength at which the current reverses direction (see Fig. 3). We point out that Fig. 4 is obtained by the TDSE model, but the density-matrix model can yield the same result. The specific details are given in Appendix B.

C. Analysis of transition channel-resolved population and photocurrent

To get deeper insight into the mechanism of the current reversal, decompositions of interband transition channels are useful. The TDSE model allows us to analyze the transition between a given pair of valence and conduction bands. In analogy to Eq. (7), we can define channel-resolved transferred charge density as

$$Q_{s,n} = \int_{\mathrm{BZ}} \rho_n^s(\mathbf{k}_0, +\infty)\mathbf{e_m} \cdot \nabla_{\mathbf{k}_0}\varepsilon_n(\mathbf{k}_0)d\mathbf{k}_0, \qquad (17)$$

which can give rise to the photocurrent originated from the nth CB whose population is contributed by the initially occupied sth VB. The superposition of $Q_{s,n}$ over all possible transition channels from VB to CB yields the total charge density.

For a convenient description below, valence (conduction) bands from the highest (lowest) to the bottom (top) are marked

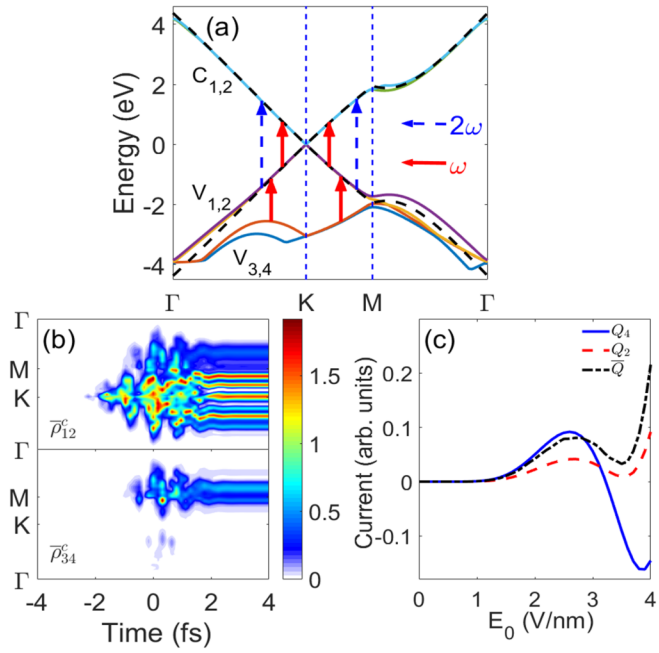

FIG. 5. (a) Electronic band structures of our tBLG around the Fermi energy. The red solid and blue dashed arrows represent single-photon and two-photon resonance positions, respectively. The black dashed line represents the MLG energy band for comparison. (b) The temporal evolution of $\bar{\rho}^c_{12}$ (top panel) and $\bar{\rho}^c_{34}$ (bottom panel) along the high-symmetry pathway under the peak field strength $E_0 = 3.5\,\mathrm{V/nm}$. (c) Comparison of three different channel-resolved currents (Q_4, Q_2, and $\bar{Q}$) as a function of E_0. Other laser parameters are the same as in Fig. 3.

successively as $V_1, V_2, \ldots$ ($C_1, C_2, \ldots$). Figure 5(a) shows the most relevant four VBs (V_1, V_2, V_3, and V_4) and two CBs (C_1 and C_2) closest to the Fermi level for tBLG ($m = 1$, $r = 1$).

We first observed the temporal evolution of a population of different CBs. Note that $\rho^s_n(\mathbf{k}_0, t)$ defined in both Eqs. (7) and (17) refers to the acceleration frame. The population evolution in the reciprocal space is better visualized within the laboratory frame, where the corresponding k-space population $\bar{\rho}^s_n(\mathbf{k}_0, t)$ is given by the relationship $\bar{\rho}^s_n(\mathbf{k}_0, t) \equiv \rho^s_n[\mathbf{k}_0 - \mathbf{A}(t), t]$. Here, the index s indicates that the electron initially occupies the sth band, and $\bar{\rho}^s_n$ represents the time-dependent population of the nth band obtained from the s-occupied initial condition. Hence, the population of $C_1 + C_2$ bands and $C_3 + C_4$ bands can be expressed, respectively, as

$$\bar{\rho}^c_{12}(\mathbf{k}_0, t) = \sum_{s\in \mathrm{VB}, n=\mathrm{C}_1,\mathrm{C}_2} \bar{\rho}^s_n(\mathbf{k}_0, t), \tag{18}$$

and

$$\bar{\rho}^c_{34}(\mathbf{k}_0, t) = \sum_{s\in \mathrm{VB}, n=\mathrm{C}_3,\mathrm{C}_4} \bar{\rho}^s_n(\mathbf{k}_0, t). \tag{19}$$

Figure 5(b) shows time-dependent population $\bar{\rho}^c_{12}$ (top panel) and $\bar{\rho}^c_{34}$ (bottom panel), calculated along the high-symmetry pathway $\Gamma - K - M - \Gamma$ for $E_0 = 3.5\,\mathrm{V/nm}$. It is found that $\bar{\rho}^c_{12}$ starts to grow from the Dirac point at the front edge of the laser pulse, then spreads to another area, and finally forms a stable residual distribution. However, $\bar{\rho}^c_{34}$ is not obvious until the laser field reaches the maximum, leading to the final distribution with the amplitude much smaller than $\bar{\rho}^c_{12}$. The result implies that the C_1 and C_2 bands dominate the photocurrent generation.

In order to further identify VB contributions, we define

$$Q_2 = \sum_{\substack{s\in\{\mathrm{V}_1,\mathrm{V}_2\}\\ n\in\{\mathrm{C}_1,\mathrm{C}_2\}}} Q^s_n, \tag{20}$$

and

$$Q_4 = \sum_{\substack{s\in\{\mathrm{V}_1,\mathrm{V}_2,\mathrm{V}_3,\mathrm{V}_4\}\\ n\in\{\mathrm{C}_1,\mathrm{C}_2\}}} Q^s_n, \tag{21}$$

which are calculated as a function of field strength. Figure 5(c) shows that calculations including four VBs (blue solid) can reproduce almost all important characteristics of field-dependent total current, same as the olive dashed dot curve in Fig. 3, while only considering two VBs (red dashed) is insufficient to capture the current direction reversal. It follows that the dynamical interaction associated with the original 28 bands in tBLG can be simplified to a six-band model (V_{1-4} and $C_{1,2}$).

We continue to analyze excitation processes among the six bands by imaging time-dependent population at a fixed $E_0 = 3.5\,\mathrm{V/nm}$. The transition from $V_{1,2}$ to $C_{1,2}$ can be characterized by

$$\bar{\rho}_a(\mathbf{k}_0, t) = \sum_{\substack{s=\mathrm{V}_1,\mathrm{V}_2\\ n=\mathrm{C}_1,\mathrm{C}_2}} \bar{\rho}^s_n(\mathbf{k}_0, t), \tag{22}$$

which is plotted in Fig. 6(a). It is evident that $\bar{\rho}_a$ first appears near the Dirac point K and subsequently spreads following the laser field oscillation, consistent with the Landau-Zener (LZ) tunneling picture. Additionally, the residual distribution of $\bar{\rho}_a$ in Fig. 6(a) suggests the existence of a single-photon and two-photon transition process if we interpret the interaction in the frequency domain, as marked by the arrow in Fig. 5(a).

For clarifying transitions from $V_{3,4}$ to $C_{1,2}$, we calculate the population of the middle VBs $V_{1,2}$,

$$\bar{\rho}_m(\mathbf{k}_0, t) = \sum_{\substack{s=\mathrm{V}_3,\mathrm{V}_4\\ n=\mathrm{V}_1,\mathrm{V}_2}} \bar{\rho}^s_n(\mathbf{k}_0, t). \tag{23}$$

The result is reported in Fig. 6(b), representing that the electron is excited from $V_{3,4}$ to $V_{1,2}$ beginning around the Γ point, where LZ tunneling easily happens due to the almost close band structure. The residual population of $\bar{\rho}_m$ in Fig. 6(b) also suggests the existence of a dominant single-photon transition process between $V_{3,4}$ and $V_{1,2}$, as marked by the arrow in Fig. 5(a).

It is expected from Fig. 6(b) that $V_{1,2}$ serves as a bridge that connects the transition between $V_{3,4}$ and $C_{1,2}$, which can be verified by comparing the total population,

$$\bar{\rho}_b(\mathbf{k}_0, t) = \sum_{\substack{s=\mathrm{V}_3,\mathrm{V}_4\\ n=\mathrm{C}_1,\mathrm{C}_2}} \bar{\rho}^s_n(\mathbf{k}_0, t), \tag{24}$$

and the direct transition population $\bar{\rho}_\mathrm{d}(\mathbf{k}_0, t)$. The latter, $\bar{\rho}_\mathrm{d}(\mathbf{k}_0, t)$, is obtained by the following procedures: During

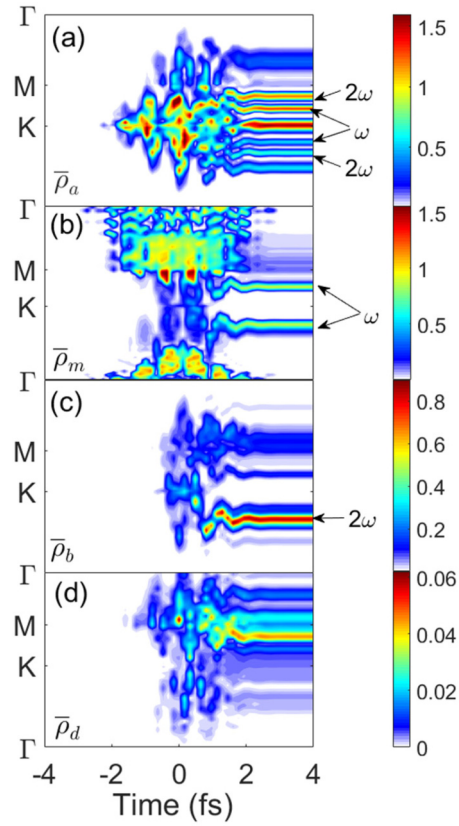

FIG. 6. The time-dependent population for (a) $\bar{\rho}_a$ transition from $V_{1,2}$ to $C_{1,2}$, (b) $\bar{\rho}_m$ transition from $V_{3,4}$ to $V_{1,2}$, (c) $\bar{\rho}_b$ transition from $V_{3,4}$ to $C_{1,2}$, and (d) $\bar{\rho}_d$ direct transition from $V_{3,4}$ to $C_{1,2}$ without passing through $V_{1,2}$. Significant single-photon and two-photon resonances are indicated on the right side. The CP laser pulse centered at 800 nm has a duration of 5 fs and a peak field strength of $E_0 = 3.5\,\mathrm{V/nm}$.

each propagation step of solving Eq. (5) at such initial condition that $V_{3,4}$ is fully occupied, $\mathbf{C}^{\mathbf{k}_0}(t)$ is transformed to band representation $\mathbf{C}_B^{\mathbf{k}_0}(t)$, followed by artificially removing populations of $V_{1,2}$, and then transformed back to atomic orbit representation $\mathbf{C}^{\mathbf{k}_0}(t)$. The process is repeated until the end of the pulse; meanwhile $\bar{\rho}_d(\mathbf{k}_0, t)$ is calculated similar to Eq. (24) but using the modified $\mathbf{C}_B^{\mathbf{k}_0}(t)$. Figures 6(c) and 6(d) show $\bar{\rho}_b(\mathbf{k}_0, t)$ and $\bar{\rho}_d(\mathbf{k}_0, t)$, respectively. The comparison of the two figures shows that removing the bridge $V_{1,2}$ will lead to dramatically reduced $\bar{\rho}_d(\mathbf{k}_0, t)$, demonstrating that $V_{1,2}$ plays a crucial role in electron transition from $V_{3,4}$ to $C_{1,2}$.

We also estimate the modified current $\bar{Q}$, defined by the situation that when the index $s \neq V_{1,2}$ in the summation of Eq. (7) the contribution of $V_{1,2}$ is removed by the same procedure as calculating $\bar{\rho}_d(\mathbf{k}_0, t)$. This treatment represents that those transitions to CBs through $V_{1,2}$ as a bridge are not considered. Afterward, the $\bar{Q}$ is plotted as a function of E_0, as shown by the black dashed-dotted line in Fig. 5(c). In this case, the current reversal disappears. Thus, the above results identify two dominant channels that contribute to the $C_{1,2}$ population, including the direct transition from $V_{1,2}$ to $C_{1,2}$ and the indirect transition from $V_{3,4}$ to $C_{1,2}$ through $V_{1,2}$.

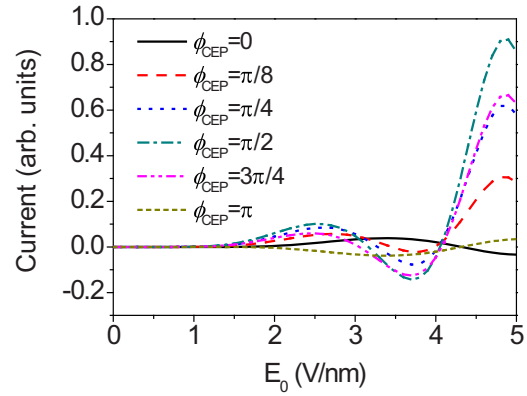

FIG. 7. The current in tBLG ($m = 1, r = 1$) as a function of peak electric field E_0, calculated for six different CEPs. Other laser parameters are the same as in Fig. 3.

The interference of two quantum pathways leads to the current direction reversal in tBLG.

D. Influence of CEP and twisted angles

In order to obtain a comprehensive observation, we have further investigated the effect of the CEP of the driving pulse and twisted angles on field-dependent current.

Figure 7 shows field strength dependent current in tBLG ($m = 1,\ r = 1$) under six different CEPs. We only plot the TDSE result, and the density-matrix model yields the same conclusion. The electrode orientation is fixed to $\theta_m = 0$. One can find that for all CEPs the phenomena of current reversal always exists. We have demonstrated that the current direction reversal mainly originates from quantum interference between direct and indirect transition channels. The different CEP values cannot break this interference picture, so the sign reversal is not dependent on CEP. However, in a strong-field regime the electron dynamics is sensitive to the full electric-field waveform. The different CEPs can lead to a different phase being involved in the transition interference process and can also affect the k-resolved asymmetry distribution of conduction band population. Therefore, for the E_0-dependent curve in Fig. 7 the current amplitude and the positon at which the sign reverses are dependent on CEP.

What makes tBLG special for the current reversal phenomena? To answer this, we first emphasize the importance of the electronic interaction between adjacent layers. We calculate the field strength dependent current for the uncoupled tBLG ($m = 1,\ r = 1$) which is defined by removing all the interlayer hopping. The result is shown in Fig. 8(a). Evidently, the current reversal disappears when the interlayer interaction is artificially set to zero, even if the twisted angle still exists.

Second, we point out that the current direction reversal can also occur at other twisted angles. For example, we investigate three different twisted angles smaller and larger than the one used in Fig. 3. Figures 8(b)–8(d) show the E_0-dependent current calculated for twisted angle $\theta = 13.2^\circ$ ($m = 2,\ r = 1$), $\theta = 18.0^\circ$ ($m = 4,\ r = 3$), and $\theta = 27.8^\circ$ ($m = 2,\ r = 3$), respectively. One can see that the current direction can reverse at these twist angles, except that the electric field position where the current reversal occurs is different. To further be

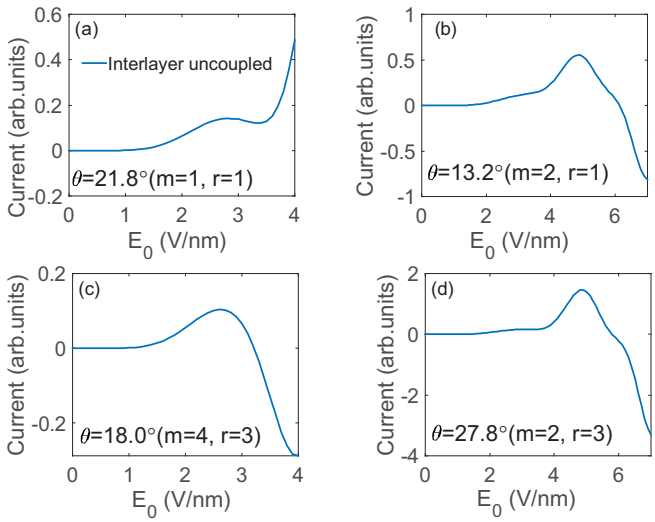

FIG. 8. (a) The current in tBLG ($m = 1,\ r = 1$) as a function of peak electric field E_0, calculated for switching off all interlayer hopping. (b–d) The current in tBLG as a function of peak electric field E_0, calculated for different twisted angles: (b) $\theta = 13.2^\circ$ ($m = 2$, $r = 1$), (c) $\theta = 18.0^\circ$ ($m = 4,\ r = 3$), and (d) $\theta = 27.8^\circ$ ($m = 2$, $r = 3$). Other laser parameters are the same as in Fig. 3.

sure that the current reversal will not occur in MLG and AA/AB bilayers, we have calculated E_0-dependent current upon scanning the field strength up to as high as 10 V/nm, and find that there are still no reversal phenomena.

According to the above analysis, we can interpret that tBLG is special due to the particular band structure. The mismatch rotation angle between two atomic layers and the interlayer interaction can introduce an additional freedom that leads to forming a moiré pattern superlattice with a higher periodicity. This property corresponds to the Brillouin zone folding in tBLG compared with MLG or AA/AB stacking. This kind of band structure supports multichannel interference including direct and indirect transition among a few bands near the Fermi level. Consequently, the current sign reversal can occur for tBLG.

IV. CONCLUSIONS

In summary, we have theoretically investigated light field induced current in the minimal commensurate tBLG, arising from the nonlinear optical response to an intense few-cycle CP pulse. The tight-binding electronic structure of tBLG is incorporated into two independent single-particle methods, i.e., a TDSE in the length-gauge and density-matrix equation in the velocity gauge, for describing the strong-field electron dynamics. The results obtained by the two models are cross-checked to ensure the validity of our simulation.

Generally, the length gauge and velocity gauge are not completely equivalent due to the inevitable approximations made in the practical calculation. It is pointed out in [28] that length gauge can avoid unphysical zero-frequency divergences and is more suitable for at least the calculation of frequency-dependent susceptibilities. In contrast, the velocity-gauge nonperturbative expression may lead to false poles and suffers from the singularity in the low-frequency regime [29]. In our work, the photon energy of an 800-nm driving field can be thought of as sufficiently high in comparison with the tBLG band gap, so that true resonances of the system are dominant and the low-frequency singularity is suppressed. At the same time, we only focus on the net photocurrent and do not care about frequency-dependent physical quantity. Consequently, our results do not depend on the use of the length-gauge or velocity-gauge approach.

We show that optically induced currents are dependent on both the electrode orientation relative to the tBLG lattice and the exact waveform of CP light field that is controlled by CEP. This kind of dependence can be fitted to the sine function with the phase determined by the algebraic sum or difference of CEP and orientation angle. The property can be also simply interpreted in terms of the semiclassical acceleration theorem. Therefore, the practical arrangement of electrodes is free, since its orientation can be simply considered as a trivial phase shift of CEP-dependent current.

We further demonstrate that photocurrent exhibits a non-monotonic behavior as optical field strength increases to the strong-field regime, even leading to a striking reversal in the current direction. This is a unique feature associated with the tBLG that is not present in a monolayer or conventional bilayers. The residual population of CBs in the reciprocal space is also calculated, which uncovers an important signature of the field strength control of electric current and the resulting reversal phenomena. Additionally, a detailed analysis of channel-resolved population and current verifies that dynamics in tBLG is predominately governed by four VBs and two CBs closest to the Fermi level. Based on this analysis, we explain the current direction reversal in tBLG as a result of quantum interference of direct and indirect transition channels. Our work reveals the promising optical and electric properties of tBLG, which might be used in future optoelectronics.

ACKNOWLEDGMENTS

This work was supported by the National Natural Science Foundation of China (Grants No. 12174413, No. 61690223, and No. 11774363) and the Strategic Priority Research Program of the Chinese Academy of Sciences (Grant No. XDB16).

APPENDIX A: DERIVATION DETAILS

In this Appendix we provide more details about the solution of the TDSE based on the tight-binding approximation. We consider a general situation that there are several atoms per unit cell and several orbitals on a given atom. In this case, the basis function that satisfies Bloch's theorem is constructed by the linear combination of atomic orbitals $\phi_{\alpha n}$ as

$$B_{\alpha,n,\mathbf{k}}(\mathbf{r}) = \frac{1}{\sqrt{N}} \sum_{\mathbf{R}} e^{i\mathbf{k}\cdot(\mathbf{R}+\tau_n)} \phi_{\alpha n}(\mathbf{r} - \mathbf{R} - \tau_n), \qquad \text{(A1)}$$

where α specifies the shape of the orbitals (s, p, etc.), n labels one atom in the primary cell, and τ_n is the location of atom n relative to the primary unit cell. Here the sum runs over lattice vectors $\mathbf{R}$, and there are N unit cells in the crystal.

By applying the basis function Eq. (A1) in a moving frame where the lattice momentum is shifted by the vector potential of the laser pulse, we can write the wave function for an initial crystal momentum $\mathbf{k}_0$ as

$$\psi_{\mathbf{k}_0}(\mathbf{r},t)=\sum_{\alpha n}c^{\mathbf{k}_0}_{\alpha,n}(t)B_{\alpha,n,\mathbf{k}(t)}(\mathbf{r}), \tag{A2}$$

with the time-dependent momentum $\mathbf{k}(t)=\mathbf{k}_0+\mathbf{A}(t)$. Differentiating both sides of Eq. (A2) with respect to t, we can get

$$\begin{aligned} i\frac{\partial\psi_{\mathbf{k}_0}(\mathbf{r},t)}{\partial t}&=i\sum_{\alpha n}\frac{\partial c^{\mathbf{k}_0}_{\alpha,n}(t)}{\partial t}B_{\alpha,n,\mathbf{k}(t)}(\mathbf{r})+\mathbf{E}(t)\cdot\sum_{\alpha n}c^{\mathbf{k}_0}_{\alpha,n}(t)\frac{1}{\sqrt{N}}\sum_{\mathbf{R}}(\mathbf{R}+\tau_n)e^{i\mathbf{k}(t)\cdot(\mathbf{R}+\tau_n)}\phi_{\alpha n}(\mathbf{r}-\mathbf{R}-\tau_n)\\ &=i\sum_{\alpha n}\frac{\partial c^{\mathbf{k}_0}_{\alpha,n}(t)}{\partial t}B_{\alpha,n,\mathbf{k}(t)}(\mathbf{r})+\mathbf{E}(t)\cdot\mathbf{r}\psi_{\mathbf{k}_0}(t)-\mathbf{E}(t)\cdot\sum_{\alpha n}c^{\mathbf{k}_0}_{\alpha,n}(t)\frac{1}{\sqrt{N}}\sum_{\mathbf{R}}(\mathbf{r}-\mathbf{R}-\tau_n)e^{i\mathbf{k}(t)\cdot(\mathbf{R}+\tau_n)}\phi_{\alpha n}(\mathbf{r}-\mathbf{R}-\tau_n). \end{aligned} \tag{A3}$$

By combining Eqs. (A3) and (3), we arrive at

$$i\sum_{\alpha n}\frac{\partial c^{\mathbf{k}_0}_{\alpha,n}(t)}{\partial t}B_{\alpha,n,\mathbf{k}(t)}(\mathbf{r})=H_0\psi_{\mathbf{k}_0}(t)+\mathbf{E}(t)\cdot\sum_{\alpha n}c^{\mathbf{k}_0}_{\alpha,n}(t)\frac{1}{\sqrt{N}}\sum_{\mathbf{R}}(\mathbf{r}-\mathbf{R}-\tau_n)e^{i\mathbf{k}(t)\cdot(\mathbf{R}+\tau_n)}\phi_{\alpha n}(\mathbf{r}-\mathbf{R}-\tau_n). \tag{A4}$$

After multiplying Eq. (A4) by $B^*_{\beta,m,\mathbf{k}}(\mathbf{r})$ and then integrating over real space, Eq. (A4) becomes

$$i\sum_{\alpha n}S_{\beta m,\alpha n}(\mathbf{k})\frac{\partial c^{\mathbf{k}_0}_{\alpha,n}(t)}{\partial t}=H_{\beta m,\alpha n}(\mathbf{k})c^{\mathbf{k}_0}_{\alpha,n}(t)+\mathbf{E}(t)\cdot\sum_{\alpha n}\mathbf{d}_{\beta m,\alpha n}(\mathbf{k})c^{\mathbf{k}_0}_{\alpha,n}(t), \tag{A5}$$

where some matrix elements are explicitly given by

$$S_{\alpha n,\beta m}(\mathbf{k})=\langle B_{\alpha,n,\mathbf{k}}(\mathbf{r})|B_{\beta,m,\mathbf{k}}(\mathbf{r})\rangle=\sum_{\mathbf{R}_{nm}}e^{i\mathbf{k}\cdot\mathbf{R}_{nm}}\langle\phi_{\alpha n}(\mathbf{r})|\phi_{\beta m}(\mathbf{r}-\mathbf{R}_{nm})\rangle, \tag{A6}$$

$$H_{\alpha n,\beta m}(\mathbf{k})=\langle B_{\alpha,n,\mathbf{k}}(\mathbf{r})|H_0|B_{\beta,m,\mathbf{k}}(\mathbf{r})\rangle=\sum_{\mathbf{R}_{nm}}e^{i\mathbf{k}\cdot\mathbf{R}_{nm}}\langle\phi_{\alpha n}(\mathbf{r})|H_0|\phi_{\beta m}(\mathbf{r}-\mathbf{R}_{nm})\rangle, \tag{A7}$$

$$\mathbf{d}_{\beta m,\alpha n}(\mathbf{k})=\sum_{\mathbf{R}_{nm}}e^{-i\mathbf{k}\cdot\mathbf{R}_{nm}}\langle\phi_{\beta m}(\mathbf{r}-\mathbf{R}_{nm})|\mathbf{r}|\phi_{\alpha n}(\mathbf{r})\rangle, \tag{A8}$$

with the definition $\mathbf{R}_{nm}=\mathbf{R}+\tau_m-\tau_n$.

We can rewrite Eq. (A5) in a matrix form without displaying the indices,

$$i\mathbf{S}(\mathbf{k})\frac{\partial}{\partial t}\mathbf{C}^{\mathbf{k}_0}(t)=[\mathbf{H}(\mathbf{k})+\mathbf{E}(t)\cdot\mathbf{d}(\mathbf{k})]\mathbf{C}^{\mathbf{k}_0}(t), \tag{A9}$$

where $\mathbf{S}(\mathbf{k})$ is called the overlap matrix, $\mathbf{H}(\mathbf{k})$ is the tight-binding Hamiltonian matrix, and $\mathbf{d}(\mathbf{k})$ is the dipole transition matrix. We notice that Eq. (A9) is a general formula. In practice, we can make some additional approximation to simply this equation. For $\mathbf{S}(\mathbf{k})$ and $\mathbf{d}(\mathbf{k})$, in the spirit of the tight-binding condition, the basic assumption is that the overlapping between atomic orbitals on different atomic sites is negligibly small. When the orbitals are further assumed to be normalized, $\mathbf{S}(\mathbf{k})$ becomes unity matrix and we have [30]

$$\langle\phi_{\beta m}(\mathbf{r}-\mathbf{R}_{nm})|\mathbf{r}|\phi_{\alpha n}(\mathbf{r})\rangle=\delta_{\mathbf{R},0}\delta_{nm}(\mathbf{R}_{nm}\delta_{\beta\alpha}+\tilde{\mathbf{d}}_{\beta\alpha}), \tag{A10}$$

where $\tilde{\mathbf{d}}_{\beta\alpha}$ represents the intra-atomic dipole matrix element. By substituting Eq. (A10) into Eq. (A8), $\mathbf{d}(\mathbf{k})$ becomes zero if the selection rule forbids the intra-atomic dipole transition.

After using these approximations, Eq. (A9) can reduce to Eq. (5), as given in the main text.

For the commensurate tBLG studied in our work, we only consider the $2p_z$ electron. The tight-binding Hamiltonian can be written as

$$H_{\mathrm{tBLG}}=\sum_{s=1}^{2}\sum_{\langle i,j\rangle}V^0_{\mathrm{pp}\pi}\hat{c}^+_{si}c_{sj}+\sum_{s=1}^{2}\sum_{ij}t^{s\bar{s}}_{ij}\hat{c}^+_{si}c_{\bar{s}j}, \tag{A11}$$

where the first term represents nearest-neighbor interactions in the graphene layer s, and the second term represents the interlayer interaction between different graphene layers s and $\bar{s}$. The hopping integral between atom i and atom j, which are in different layers, is given by the following formula based on the Slater-Koster mechanism [24,31]:

$$t_{ij}=V^0_{\mathrm{pp}\pi}\exp\left(-\frac{|\mathbf{R}_{ij}|-a_{cc}}{\lambda}\right)\cdot\left[1-\left(\frac{\mathbf{R}_{ij}\cdot\mathbf{e}_z}{|\mathbf{R}_{ij}|}\right)^2\right]+V^0_{pp\sigma}\exp\left(-\frac{|\mathbf{R}_{ij}|-d_0}{\lambda}\right)\cdot\left(\frac{\mathbf{R}_{ij}\cdot\mathbf{e}_z}{|\mathbf{R}_{ij}|}\right)^2, \tag{A12}$$

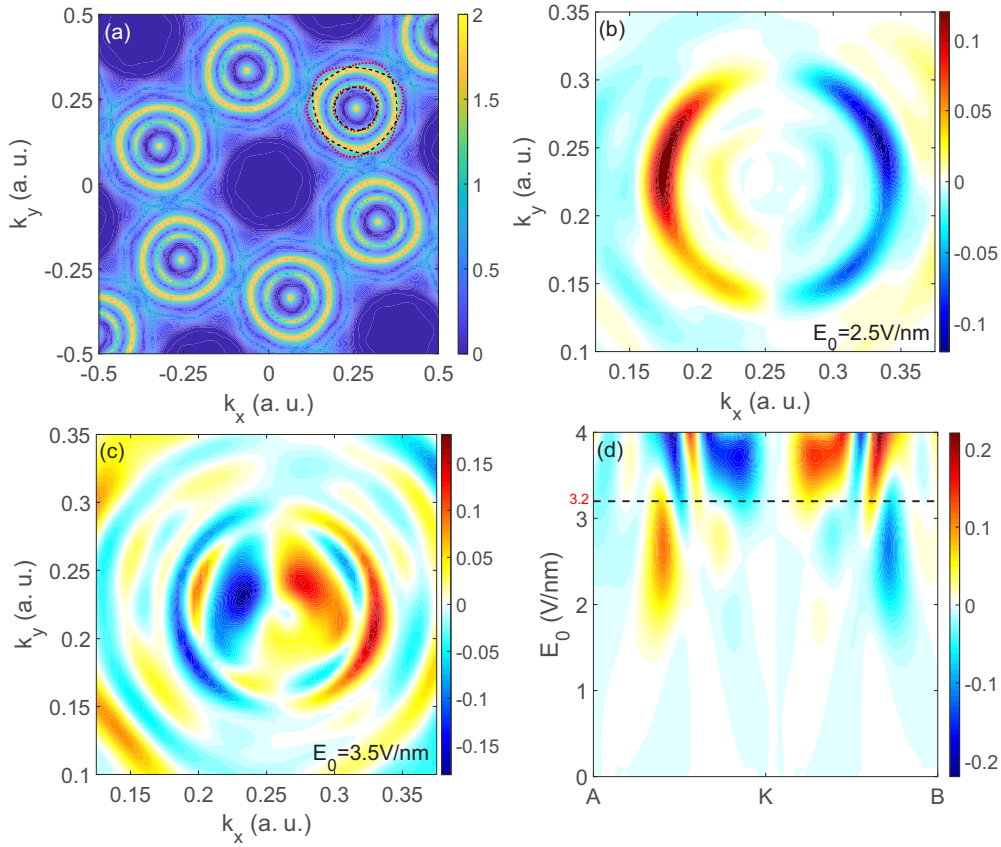

FIG. 9. (a) The k-resolved residual distribution of total CB population for $E_0 = 3.5\,\mathrm{V/nm}$. Black dashed (red dotted) curves around one of the Dirac points represent resonances, where the energy difference between the lowest (the second lowest) CB and the highest (the second highest) VB is equal to photon energy $\hbar\omega_0$ or $2\hbar\omega_0$. (b), (c) The difference $\Delta\rho_c(\mathbf{k}_0)$ between the residual CB population resulting from excitation with $\phi_{\mathrm{CEP}} = \pi/2$ and $\phi_{\mathrm{CEP}} = -\pi/2$, plotted at two different peak field strengths (b) $E_0 = 2.5\,\mathrm{V/nm}$ and (c) $E_0 = 3.5\,\mathrm{V/nm}$. (d) Extracted $\Delta\rho_c(\mathbf{k}_0)$ along a straight line denoted by AKB in Fig. 4(c), calculated as a function of E_0. The black dashed line indicates the field strength $E_0 = 3.2\,\mathrm{V/nm}$ at which the current direction reverses. Other laser parameters are the same as in Fig. 3.

where $V^0_{\mathrm{pp}\pi}$ is the hopping integral for two vertically located atoms in the adjacent layers, d_0 is the distance between graphene layer s and $\bar{s}$, λ modulates the decay of hopping integral at the large distance, and $\mathbf{e}_z$ is the unit vector perpendicular to the tBLG plane. In our simulation, these parameters are $V^0_{\mathrm{pp}\pi} = -3.03\,\mathrm{eV}$, $V^0_{\mathrm{pp}\sigma} = 0.39\,\mathrm{eV}$, $d_0 = 3.35\,\mathrm{Å}$, and $\lambda = 0.27\,\mathrm{Å}$.

Different from many previous works, we establish a full Hamiltonian for tBLG without using low-energy continuum approximation, and numerically obtain all energy bands through a complete diagonalization algorithm. As for large-angle tBLG, the $U(1)_v$ symmetry can be broken, and the intervalley coupling can result in the increased band gap opening between Dirac points as the twist angle θ increases. Indeed, our tight-binding model can lead to such a gap of about 4 meV at $\theta \approx 21.8^\circ$ ($m = 1$, $r = 1$). This gap value is similar to the previous result, 3–9 meV, reported in Refs. [25,32]. Additionally, our model can support the first magic angle $\theta \approx 1.08^\circ$ at which band flattening occurs and simultaneously reveals the fact that the Fermi velocity monotonously decreases with decreasing twist angle [21]. There characteristics are quite consistent with many previous studies utilizing different approaches [23,33,34], thus demonstrating the validity of the model.

To check the robustness of results to the tight-binding parameters, we have used another set of parameters, which are taken from [24], i.e., $V^0_{\mathrm{pp}\pi} = -2.7\,\mathrm{eV}$, $V^0_{\mathrm{pp}\sigma} = 0.48\,\mathrm{eV}$, and $\lambda = 0.453\,\mathrm{Å}$. They are increased by 12.6%, 23%, and 67%, respectively, in comparison with our used values. We find the result and conclusion in this work are robust against the variation of tight-binding parameters.

APPENDIX B: DENSITY-MATRIX CALCULATION CORRESPONDING TO FIG. 4

For the density-matrix model, the population calculation is much easier in comparison with the TDSE model. The diagonal elements of the density matrix represent the population on each energy band. Thus, the residual CB population can be directly obtained by summing the required diagonal elements at the end of the pulse. We perform the same calculation corresponding to Fig. 4. The results are reported in Fig. 9. One can see that almost the same distribution is present as in Fig. 4.

[1] E. Goulielmakis, V. S. Yakovlev, A. L. Cavalieri, M. Uiberacker, V. Pervak, A. Apolonski, R. Kienberger, U. Kleineberg, and F. Krausz, Science **317**, 769 (2007).

[2] F. Krausz and M. I. Stockman, Nat. Photon. **8**, 205 (2014).

[3] H. Mashiko, K. Oguri, T. Yamaguchi, A. Suda, and H. Gotoh, Nat. Phys. **12**, 741 (2016).

[4] A. Schiffrin, T. Paasch-Colberg, N. Karpowicz, V. Apalkov, D. Gerster, S. Mühlbrandt, M. Korbman, J. Reichert, M. Schultze, S. Holzner, J. V. Barth, R. Kienberger, R. Ernstorfer, V. S. Yakovlev, M. I. Stockman, and F. Krausz, Nature (London) **493**, 70 (2013).

[5] O. Kwon, T. Paasch-Colberg, V. Apalkov, B. K. Kim, J. J. Kim, M. I. Stockman, and D. Kim, Sci. Rep. **6**, 21272 (2016).

[6] O. Kwon and D. Kim, Appl. Phys. Lett. **108**, 191112 (2016).

[7] T. Paasch-Colberg, S. Yu. Kruchinin, Ö. Sağlam, S. Kapser, S. Cabrini, S. Muehlbrandt, J. Reichert, J. V. Barth, R. Ernstorfer, R. Kienberger, V. S. Yakovlev, N. Karpowicz, and A. Schiffrin, Optica **3**, 1358 (2016).

[8] G. Wachter, C. Lemell, J. Burgdorfer, S. A. Sato, X. M. Tong, and K. Yabana, Phys. Rev. Lett. **113**, 087401 (2014).

[9] O. Kwon and D. Kim, J. Opt. Soc. Am. B **37**, 3429 (2020).

[10] S. Yu. Kruchinin, M. Korbman, and V. S. Yakovlev, Phys. Rev. B **87**, 115201 (2013).

[11] S. Sederberg, F. Kong, F. Hufnagel, C. Zhang, E. Karimi, and P. B. Corkum, Nat. Photon. **14**, 680 (2020).

[12] C. Heide, T. Boolakee, T. Higuchi, H. B. Weber, and P. Hommelhoff, New J. Phys. **21**, 045003 (2019).

[13] T. Higuchi, C. Heide, K. Ullmann, H. B. Weber, and P. Hommelhoff, Nature (London) **550**, 224 (2017).

[14] T. Boolakee, C. Heide, F. Wagner, C. Ott, M. Schlecht, J. Ristein, H. B. Weber, and P. Hommelhoff, J. Phys. B: At. Mol. Opt. Phys. **53**, 154001 (2020).

[15] E. Wu, C. Zhang, Z. Wang, and C. Liu, New J. Phys. **22**, 033016 (2020).

[16] Y. Cao, V. Fatemi, S. Fang, K. Watanabe, T. Taniguchi, E. Kaxiras, and P. Jarillo-Herrero, Nature (London) **556**, 43 (2018).

[17] Y. Cao, V. Fatemi, A. Demir, S. Fang, S. L. Tomarken, J. Y. Luo, J. D. Sanchez-Yamagishi, K. Watanabe, T. Taniguchi, E. Kaxiras, R. C. Ashoori, and P. Jarillo-Herrero, Nature (London) **556**, 80 (2018).

[18] B. Deng, C. Ma, Q. Wang, S. Yuan, K. Watanabe, T. Taniguchi, F. Zhang, and F. Xia, Nat. Photonics **14**, 549 (2020).

[19] Y. Gao, Y. Zhang, and D. Xiao, Phys. Rev. Lett. **124**, 077401 (2020).

[20] T. N. Ikeda, Phys. Rev. Res. **2**, 032015(R) (2020).

[21] M. Du, C. Liu, Z. Zeng, and R. Li, Phys. Rev. A **104**, 033113 (2021).

[22] J. M. B. Lopes dos Santos, N. M. R. Peres, and A. H. Castro Neto, Phys. Rev. Lett. **99**, 256802 (2007).

[23] J. M. B. Lopes dos Santos, N. M. R. Peres, and A. H. Castro Neto, Phys. Rev. B **86**, 155449 (2012).

[24] P. Moon and M. Koshino, Phys. Rev. B **87**, 205404 (2013).

[25] A. O. Sboychakov, A. L. Rakhmanov, A. V. Rozhkov, and F. Nori, Phys. Rev. B **92**, 075402 (2015).

[26] A. Haché, Y. Kostoulas, R. Atanasov, J. L. P. Hughes, J. E. Sipe, and H. M. van Driel, Phys. Rev. Lett. **78**, 306 (1997).

[27] D. Sun, C. Divin, J. Rioux, J. E. Sipe, C. Berger, W. A. de Heer, P. N. First, and T. B. Norris, Nano Lett. **10**, 1293 (2010).

[28] C. Aversa and J. E. Sipe, Phys. Rev. B **52**, 14636 (1995).

[29] K. S. Virk and J. E. Sipe, Phys. Rev. B **76**, 035213 (2007).

[30] M. Cruz, M. R. Beltrán, C. Wang, J. Tagüeña-Martínez, and Y. G. Rubo, Phys. Rev. B **59**, 15381 (1999).

[31] H. A. Le and V. N. Do, Phys. Rev. B **97**, 125136 (2018).

[32] M. J. Park, Y. Kim, G. Y. Cho, and S. B. Lee, Phys. Rev. Lett. **123**, 216803 (2019).

[33] S. Shallcross, S. Sharma, E. Kandelaki, and O. A. Pankratov, Phys. Rev. B **81**, 165105 (2010).

[34] S. Fang and E. Kaxiras, Phys. Rev. B **93**, 235153 (2016).